Published in final edited form as:

Addit Manuf. 2023 June 05; 71: . doi:10.1016/j.addma.2023.103589.

Simultaneous rheology and cure kinetics dictate thermal post-curing of thermoset composite resins for material extrusion[1]

Stian K. Romberg,

Anthony P. Kotula

Materials Science and Engineering Division, National Institute of Standards and Technology, Gaithersburg, MD 20899

Abstract

Thermoset composites are excellent candidates for material extrusion because they shear thin during extrusion but retain their shape once deposited via a yield stress. However, thermal post-curing is often required to solidify these materials, which can destabilize printed parts. Elevated temperatures can decrease the rheological properties responsible for stabilizing the printed structure before crosslinking solidifies the material. These properties, namely the storage modulus and yield stress, must therefore be characterized as a function of temperature and extent of reaction for various filler loadings. This work utilizes rheo-Raman spectroscopy to measure the storage modulus and dynamic yield stress as a function of temperature and conversion in epoxy-amine resins with fumed silica mass fractions up to 10 %. Both rheological properties are sensitive to conversion and particle loading, but only the dynamic yield stress is reduced by elevated temperatures early in the cure. Notably, the dynamic yield stress increases with conversion well before the chemical gel point. These findings motivate a two-step cure protocol that starts at a low temperature to mitigate the drop in dynamic yield stress, then ramps up to a high temperature when the dynamic yield stress is no longer at risk of decreasing to rapidly drive conversion to near completion. The results suggests that structural stability can be improved without resorting to increasing filler content, which limits control over the final properties, laying the groundwork for future studies to evaluate the stability improvements provided by the multi-step curing schedules.

Keywords

rheo-Raman; thermoset composite; yield stress fluid; direct ink writing; thermal post-cure

1 Introduction

The unique yield stress and shear-thinning behavior of thermoset composite resins has enabled a wide variety of thermally post-cured material extrusion (also known as direct ink writing), but the limited structural stability provided by the rheological properties of these resins has restricted their application to the benchtop scale [1–13]. Adding more nanofiller to the thermoset matrix can improve shape retention and structural stability, but

[1]Official contribution of the National Institute of Standards and Technology; not subject to copyright in the United States.

corresponding author: anthony.kotula@nist.gov.

this can make the material more resistant to extrusion [14]. Therefore, efforts to print larger parts typically utilize in-process curing to overcome structural instability [13, 15–33]; however, the scale that necessitates this more complicated approach remains in question. The evolving rheological properties of thermoset composite resins during thermal post-curing, one of the most widespread and simplest alternatives to in-process curing, must be characterized to address this question. Properties do not necessarily monotonically increase during the curing process. Once heat is applied, rheological properties can drop below their room-temperature value before crosslinking can solidify the material [34–38], resulting in collapse of prints that remained stable during the room-temperature printing process [39–41]. Clearly, temperature effects and crosslinking compete to govern rheological properties, and therefore structural stability. To determine the maximum feasible scale of thermally post-cured material extrusion and tailor curing schedules to enhance it, the relationship between extent of reaction, temperature, and rheological properties must be elucidated.

The extent of reaction, often measured as conversion, can be monitored using infrared or Raman spectroscopy [42, 43]. These techniques are typically applied independently of rheological testing. Variations between sample composition and thermal conditions can significantly affect reaction kinetics, leading to uncertainty when correlating spectroscopically measured conversion and rheological properties of separate samples [44–47]. To address this issue, several multimodal rheometers have been developed which incorporate infrared [44–51] or Raman spectrometers [52–56] to simultaneously control temperature, measure rheological properties, and monitor conversion for a single sample. These simultaneous measurements provide a promising way to directly link the rheological properties that are key to structural stability with the thermal curing of printable thermoset composite resins.

Many printable composite resins are formulated by adding filler particles, like fumed silica [3–6, 13, 18–20, 22–24, 30, 40, 57–59], to a thermoset matrix. These particles can form a fractal, stress-supporting network within the thermoset, creating a shear-thinning physical gel that exhibits thixotropy [60], a storage modulus (G') that exceeds the loss modulus (G'') in the linear viscoelastic regime, and a yield stress (τ_y). The storage modulus and yield stress have been experimentally linked to collapse in material extrusion [57, 58]. Increasing filler content is one way to increase these properties and enhance stability, but this approach has two important disadvantages. First, the material becomes harder to extrude, decreasing the maximum processing speed. Second, the final properties are constrained by the amount of filler required to maintain stability. The temperature dependence of thermoset properties [34, 35, 39] suggest that tailoring the curing schedule may provide an alternative way to improve stability without changing the filler content or implementing in-process curing. Executing this approach requires knowledge of how the yield stress and storage modulus evolve with temperature and conversion. The storage modulus can be tracked using small amplitude oscillatory shear (SAOS), but tracking the yield stress is less straightforward. Flow must be achieved to measure the yield stress, which introduces thixotropic effects on any subsequent testing. Obtaining the evolution of the yield stress is a key challenge that may uncover what governs structural stability during the cure.

The present work uses amine-cured epoxies with a range of fumed silica content to achieve two goals. First, to determine which rheological property causes collapse during curing, we conducted simultaneous measurements of rheology and Raman spectroscopy using a rheo-Raman instrument [54]. Using a novel protocol designed to minimize thixotropic effects, we found that the yield stress is highly sensitive to temperature and is likely the cause of collapse. Second, we used the resulting conversion-temperature-yield stress relationship to design a curing schedule to maintain the yield stress and structural stability while preserving processing speed and promoting final conversion. This demonstration suggests that stability during the cure can be improved without increasing filler content. By directly linking rheological properties to temperature and conversion, this work builds a framework to understand the size limitations caused by structural instability during thermal post-curing and presents a method to control temperature to avoid drops in properties associated with instability.

2 Materials and methods

2.1 Material formulation

Epon 826 (Hexion, Ohio, USA),[2] a diglycidyl ether of bisphenol A (DGEBA) epoxy resin, and Jeffamine D-230 (Huntsman Corporation, Texas, USA) were purchased and used as-received. The chemical structures of these materials are shown in Figure 1. Epon 826 has a functionality of two, with an epoxide equivalent mass ranging from (178 to 186) g/eq. Jeffamine D-230 has a functionality of four, with an amine hydrogen equivalent mass of 60 g/eq. Stoichiometric formulations were prepared by combining 3 g of Epon 826 with 1 g of Jeffamine D-230. Previous works on similar DGEBA-amine systems report the glass transition temperature of the fully cured material to range from (80 to 91.4) °C [68–71]. Composite resins were formulated by adding CAB-O-SIL TS-720 (Cabot Corporation, Massachusetts, USA), a hydrophobic fumed silica surface treated with polydimethylsiloxane (PDMS), to the epoxy-amine system. The primary particle size of CAB-O-SIL TS-720 ranges from (7 to 40) nm [72–74]. Primary particles interact to form aggregates on the order of 100 nm [73, 75]. Depending on the fumed silica volume fraction, fumed silica aggregates can agglomerate through particle-particle interactions to form a physical gel (with a fractal, stress-supporting network) that exhibits a nonzero storage modulus and yield stress [5, 57, 60–67]. Three resins with fumed silica mass fractions of 0 % (“neat”), 5 %, and 10 % were studied here. Previous research has shown that Epon 826 with either 5 % or 10 % fumed silica exhibits the key parameters needed for material extrusion additive manufacturing. Both filled resins shear thin, allowing for extrusion at low pressures, and exhibit a yield stress, enabling shape retention after deposition at room temperature [5, 57, 58, 76]. Although the behavior of both filled resins suggests excellent printability, only the resin filled with 10 % was printed in previous studies. A preliminary printing experiment on a custom-built printer [77], shown in Figure S1, confirmed that the 5 % fumed silica resin could be printed up to at least 10 mm in height using a 0.872 mm tapered nozzle. The

[2]Certain commercial equipment, instruments, or materials are identified in this paper in order to specify the experimental procedure adequately. Such identification is not intended to imply recommendation or endorsement by the National Institute of Standards and Technology, nor is it intended to imply that the materials or equipment identified are necessarily the best available for the purpose.

fumed silica content was varied here to evaluate how filler content affects the evolution of rheological properties during curing at elevated temperatures.

Prior to preparing the resins, Epon 826 was heated in an oven at 55 °C (if crystals were visible) for approximately 25 min until crystals were no longer observed, then cooled to room temperature. To prepare the resins, the epoxy and amine were added to a 10 cm^3 cup and mixed at a rotational frequency of 25 s^{-1} for 180 s in a centrifugal planetary mixer (Speedmixer DAC 400.2 VAC-P, FlackTek, Inc., South Carolina, USA). Fumed silica was then added to the epoxy-amine and mixed at 25 s^{-1} for 90 s. Then, material was scraped off the walls of the cup, recombined, and remixed at 25 s^{-1} for 90 s to improve homogeneity. The cup remained cool to the touch after each mixing step, indicating that the mixing did not accelerate the reaction by heating the material.

To evaluate behavior in the absence of crosslinking, additional composite resins were formulated without the amine curing agent. The resin with 5 % fumed silica was mixed using the same protocol described in the previous paragraph (two rounds of mixing at 25 s^{-1} for 90 s). At 10 %, the fumed silica was harder to disperse without the low viscosity curing agent. Therefore, this formulation was mixed at 25 s^{-1} for 90 s three times, followed by 42 s^{-1} for 90 s twice.

2.2 Rheo-Raman measurements

Simultaneous rheological and Raman measurements were performed using the rheo-Raman microscope described in previous work [54]. This instrument consists of a temperature-controlled rheometer (HAAKE MARS, Thermo Fisher Scientific, Massachusetts, USA) with a transparent base and custom optical train that allows a Raman microscope (DXR, Thermo Fisher Scientific, Massachusetts, USA) to capture spectra during rheological measurements. Raman spectra were obtained using a 10 mW laser with a wavelength of 532 nm.

Samples were measured using disposable parallel plates. The upper plate was a 20 mm diameter aluminum plate, and a disposable lower plate was created by adhering a temperature resistant quartz sheet (7784N11, McMaster-Carr Supply Company, USA) to the transparent rheometer base plate using high tack fish glue (Luthiers Mercantile International Inc., USA) (Figure S2). Both the quartz sheet and the fish glue exhibit negligible Raman scattering compared to the resins studied here. The fish glue is water soluble, so the reusable transparent base was removed from the quartz sheet and the cured sample by leaving it in water overnight. The compliance of the fish glue causes error in the measurement of the dynamic moduli, which can be quantified using analysis presented by McKenna and coworkers [78]. Figure S3 presents the error, which is small before gelation, given the parameters listed in Table S1–S2. Corrections have only been made for the SAOS results presented here. The dynamic yield stress measurements were not corrected because they exceed the linear viscoelastic regime where SAOS measurements become unreliable. Further, almost all the dynamic yield stress measurements were captured before gelation where the error is low.

SAOS experiments were conducted on the neat resin at a gap height of 1 mm and isothermal temperatures of 70 °C and 100 °C. These temperatures are below and above the reported

glass transition temperature of the fully cured material, respectively. This approach shows how curing at lower temperature affects rheological properties early in the cure but may induce vitrification and reduce conversion late in the cure. The resin was loaded between the plates near room temperature, heated to the prescribed cure temperature at a rate of 10 °C/min, then held at temperature for approximately 4 h. SAOS data was obtained from the start of the temperature ramp at a frequency of 1 Hz and strain amplitude, γ, of 0.005. Raman spectra were captured from the start of the temperature ramp. Each spectrum was averaged from two consecutive 5 s exposures.

Filled resins required a modified SAOS protocol. The filled resins are sensitive to shear history [57], so a conditioning step was added before the temperature ramp to control the initial state of the filled resins. Conditioning included shearing at a rate of 0.1 s^{-1} for 120 s and holding the material in the linear viscoelastic regime ($\gamma \leq 0.002$) for 120 s to allow it to equilibrate before ramping to the isothermal temperature. The addition of the fumed silica particles increased turbidity in the sample, decreasing the intensity of the Raman signal. Therefore, two consecutive 30 s spectra were averaged together for each reported spectrum. These parameters are summarized in Table S3 of the Supplementary Material.

Oscillatory shear stress amplitude sweeps were conducted on filled resins at room temperature and during curing. These sweeps were performed at a frequency of 1 Hz and at magnitudes ranging from 1 Pa to 10^5 Pa. The amplitude increments and stress ranges used for these measurements depended on fumed silica loading. These values are provided in Table S4 of the Supplementary Material. As shown in [57], higher amounts of large amplitude oscillatory shear result in greater thixotropic hysteresis for resins filled with fumed silica. Therefore, these large stresses should be limited to reduce thixotropic effects throughout these measurements. Stress sweeps were terminated when $\tan \delta > 1$ (i.e., when the shear loss modulus, G'', exceeded the shear storage modulus, G'), and the dynamic yield stress was measured from the logarithmically interpolated intersection of G' and G'' (interpolations are illustrated by the lines in Supplementary Material Videos S1–S4). After each sweep, the filled resin was allowed to recover for 120 s, while being monitored under SAOS. To reduce the contribution of shear history to differences in the dynamic yield stress at room temperature and the cure temperature, six measurements were conducted at room temperature before the sample was heated to the cure temperature and the dynamic yield stress measurements were resumed. The Raman spectra acquisition settings were identical to those used during SAOS measurements of the filled systems.

2.3 Rheology without curing agent

A single stress amplitude sweep was conducted on each filled resin without curing agent at room temperature and 100 °C. The same conditioning protocol (steady shear at 0.1 s^{-1} for 120 s, followed by 120 s of equilibration), stress amplitude values (Table S4), frequency (1 Hz), and termination criterion ($\delta > 1$) were used. After termination, recovery was observed for 900 s. To avoid thixotropic effects, separate samples were used for each temperature. However, each sample was taken from the same batch to eliminate differences caused by batch-to-batch variation.

The data associated with this paper is available at ref. [79].

3 Results

3.1 Calculating conversion from the Raman spectra

Raman spectra of the neat resin curing at 70 °C are shown in Figure 2a after baseline correction using the adaptive iteratively reweighted penalized least squares (airPLS) algorithm from Zhang et al. [80]. To correct for absolute intensity variations during curing we normalize each spectrum by the integrated intensity of the *gem*-dimethyl peak centered at 1187 cm^{-1}. The *gem*-dimethyl group does not take part in the reaction, and therefore this normalization allows for quantitative comparison of Raman spectra taken at different points throughout the reaction [42, 43, 55, 56, 81]. The normalized Raman spectra exhibit a decrease in peak intensity in the region of the spectrum associated with the epoxy ring stretching vibrational modes. These peaks (located at approximately 1230 cm^{-1} and 1255 cm^{-1}) [42, 43, 52, 56, 81, 82] were fit using two Gaussians and a linear baseline to measure the integrated intensity as a function of time $I(t)$ (Figure 2b). In the spectra shown here (and throughout this work), $t = 0$ s represents the time when the rheometer first reached the cure temperature. The integrated intensity allows the conversion α to be tracked throughout the experiment using the following equation

$$\alpha = 1 - \frac{I(t) - I_{FC}}{I_i - I_{FC}} \quad (1)$$

where I_i is the integrated intensity of the epoxy peaks when no crosslinking has occurred and I_{FC} is the integrated intensity of the epoxy peaks after the material has been fully cured. I_i is approximated by taking the maximum integrated intensity observed in all samples of a given rheological test set. I_{FC} cannot be assumed to be 0 because functional groups that do not take part in the epoxy-amine reaction also generate responses in this wavenumber range [56, 82]. Therefore, I_{FC} is found by measuring the Raman spectrum of a neat sample of approximately 14 mm × 8 mm × 1 mm that was cured in a silicone mold at 110 °C for 24 h to ensure the material reached full cure.

3.2 SAOS

Figure 3a shows the evolution of the storage modulus during curing for both neat and filled resins at the two cure temperatures. Although the initial G' of the neat resin is below the rheometer measurement threshold (approximately 30 Pa), the material stiffens as the resin cures and G' increases by orders of magnitude at a rate dictated by the cure temperature. At 100 °C, the storage modulus of the neat resin exhibits a rapid increase around 900 s, then plateaus to magnitudes below 10^7 Pa. The storage modulus of the neat resin cured at 70 °C exhibits a double-sigmoidal time dependence characterized by an initial rise in G' near 4000 s, an intermediate period when the modulus is of order 10^6 Pa, and a final rise in G' to magnitudes exceeding 10^7 Pa. The transitions occur at approximately the same time for the filled resins, indicating that the fumed silica does not significantly affect the rheological signature of the crosslinking process. However, the addition of fumed silica generates a resolvable G' at early times in the cure process that increases by more than an

order of magnitude when the particle loading doubles from 5 % to 10 %, which is likely due to interparticle interactions of the fumed silica [5, 57, 60–67]. Cure temperature has a negligible effect on the magnitude of G' early in the cure, as evidenced from the overlap in storage moduli for a given fumed silica loading with G'_{RT}, the storage modulus measured at room temperature prior to curing.

The critical gel point of a crosslinking material is best defined by the frequency-independence of the loss tangent, as shown by Winter and Chambon [62, 83–89]. However, some filled systems, like the physical gels presented here, do not exhibit the rheological signature of a critical gel [62, 90–93], and it is therefore necessary to use alternative metrics based on G'' (Figure 3b) and tan δ (Figure 3c). Enns and Gillham presented an alternative metric to approximate both gelation and vitrification that uses G'' versus time – gelation occurs at the “shoulder”, and vitrification occurs at the peak [94]. A clearly visible shoulder in G'' is observed near 1000 s for samples cured at the higher temperature, while a more gradual shoulder is seen around 5000 s for the samples cured at the lower temperature independent of particle loading. A vitrification peak in G'' occurs for samples cured at 70 °C at a cure time (about 10000 s) that is also independent of particle loading. Vitrification is expected under these conditions since the lower cure temperature falls below the glass transition temperature of the fully cured material, whereas the higher cure temperature exceeds the fully cured glass transition temperature [68–71, 94]. Figure 3b also reveals a large reduction in G'' after reaching the cure temperature, as shown by comparing G'' to G''_{RT}, the loss modulus measured at room temperature prior to curing.

Critical rheological transitions are also observed in the time evolution of tan δ for the filled resins (Figure 3c), which exhibits local maxima at similar times where gelation and vitrification are observed via G''. A gelation peak is absent from the tan δ of the neat resin; instead, gelation (measured from G'') occurs near the time when tan δ approaches unity [95]. This is consistent with critical percolation via chemical crosslinking in a reactive system with balanced stoichiometry [83–85]. Although the magnitude of tan δ varies prior to the gel point, tan δ follows dynamics governed by the cure temperature, and not particle loading, after gelation.

Figure 3d presents the evolution of conversion during curing. The reaction occurs faster at 100 °C than 70 °C, in agreement with the rheological measurements. Additionally, the higher temperature results in greater final conversion because it avoids vitrification which causes the reaction to become diffusion-limited [94]. At each temperature the kinetics and overall conversion is independent of filler loading. This reconfirms that reaction kinetics are not particularly sensitive to the fumed silica content. Hydroxyl groups – which are known to catalyze the reaction [52, 96] and exist on the surface of the fumed silica – are covered by a PDMS surface treatment, rendering the fumed silica chemically inert. This insensitivity enables experiments at different filler concentrations that are independent of changes in kinetics.

Simultaneous measurement enables rheological properties to be described as a function of conversion. The conversion was first smoothed using an 11-point centered moving average,

then interpolated at the times rheological properties were measured. Assuming the shoulder in G'' corresponds to gelation, Figure 4a shows that the gel point occurs at an average conversion of 0.69 ± 0.02 and is largely independent of cure temperature and particle loading. This conversion exceeds the prediction from Flory-Stockmeyer theory, which for a diepoxy-diamine blend should occur when conversion reaches 0.58. Gelation at conversion beyond the Flory-Stockmeyer prediction is not uncommon and has been observed in prior studies on diepoxy-diamine resins [94, 95]. This disagreement is attributed to intramolecular bonding and dangling chains that occur in real systems, which do not contribute to the formation of a space-spanning network and are not accounted for in the theory [95, 97]. The peak in G'' indicates that vitrification occurs at an approximate conversion of 0.85 when the samples are cured at 70 °C.

Figure 4b reveals that the stiffening of the filled resins is primarily due to the crosslinking reaction occurring in the matrix. Prior to vitrification, G' shows similar dependence on α at both cure temperatures, with the initial rise in G' occurring in all samples when $0.6 < \alpha < 0.8$. Since fumed silica is an inert filler, it does little to modify the conversion dependence of the modulus in this region. Much larger differences occur upon vitrification of the materials cured at 70 °C with the storage modulus exceeding 10^7 Pa at a reduced final conversion around 0.9. The materials cured at 100 °C do not experience vitrification and are able to reach conversion much closer to 1. Although vitrification is not expected to affect structural stability, it affects final conversion which plays a role in the final mechanical properties.

3.3 Stress sweeps

At stresses exceeding the yield stress a material will deform readily, and we expect this parameter to be a function of temperature and the extent of reaction. Characterizing the yield stress as a function of conversion *during* crosslinking requires time-resolved rheometry that 1) is rapid and 2) does not significantly perturb the filled resin microstructure. What constitutes “rapid” can be considered from the concept of a mutation number developed by Winter and coworkers [87, 98]: the timescale of the measurement should be short relative to the timescale over which the material is changing. Measurements of the yield stress can also probe well into steady flow or nonlinear oscillatory regimes where structure is necessarily broken down and a requisite recovery time must be performed after the test to allow the structure to re-form [57]. Although these recovery periods do not affect the mutation number, they do affect the rate at which measurements can be repeated and should be minimized to improve the time resolution of the data. Given the need for rapid measurements, we can neglect methods using steady flow, start-up flows, creep, or stress relaxation, since these could require long times and be difficult to assess as the material evolves with additional curing. The kinetic crosslinking process also provides challenges for oscillatory measurements depending on how the yield stress is measured. Methods that use G' or G'' as a function of amplitude to determine a yield stress (such as the maximum in G'' [99] or the deviation from linear viscoelasticity [62, 89] determined by the intersection of the low- and high-stress G' dependencies [99]) require multiple amplitude measurements to ensure accuracy, which often leads to long measurement times [99].

We avoid long measurement timescales by defining a dynamic yield stress (τ_f) from the $G' - G''$ crossover [89] during oscillatory stress amplitude sweeps at a frequency of 1 Hz. Under these conditions, we can define a mutation number as $N_{mu} = \Delta t \ \partial(\ln \tau_f)/\partial t$ [87], where Δt is the time duration for the measurement at the stress amplitude where the crossover occurs (i.e., the total time required to measure the moduli at the last amplitude below and the first amplitude above τ_f). For the results shown below, the maximum N_{mu} is approximately 0.05 (Figure S4), which satisfies the criterion $N_{mu} < 0.1$ for negligible mutation effects *during* the measurement. As defined here, this dynamic yield stress is often the largest reported "yield stress" from rheological measurements [99] and is an overestimate of the static yield stress (i.e., the stress associated with the onset of nonlinearities [89]) that governs structural collapse of printed parts caused by yielding [57]. However, determining the onset of nonlinearities requires multiple measurements in the linear range to identify where deviations from linearity first occur, which requires much longer Δt than the duration used to measure the τ_f defined here. The high amplitude stresses used in quantifying τ_f necessarily break down the network that generates the yield stress, and we therefore incorporate a 120 s rest period between amplitude sweeps to allow for network regeneration. During this period, G' shows a fast initial recovery, then begins to plateau. The stress sweeps used to measure τ_f and the recovery periods are included in the Supplementary Material (Videos S1–S4).

Figure 5 shows τ_f as a function of time for the filled resins. Negative times correspond to repeated amplitude sweeps performed at room temperature, prior to heating the sample to the cure temperature (where $t = 0$ s once the cure temperature is reached). The dynamic yield stress decreases after the first room-temperature measurement for all samples, indicating that these systems do not achieve complete recovery between measurements. However, all samples reach or approach a reduced steady state value of τ_f during the repeated room-temperature sweeps. The steady state τ_f provides a measurement that accounts for shear history and a better comparison for the dynamic yield stress measurements conducted on partially recovered material at the elevated cure temperatures. Ideally, yield stress tests would be conducted only when the material has recovered to its initial state. However, this is impractical for this material system because the recovery period is extremely long. Previous work shows that at room temperature, the storage modulus of these composite resins without curing agent is far from full recovery, even after 15 minutes [57]. For the filled resins with 5 % fumed silica a steady state value of τ_f near 10^2 Pa is observed. Doubling the particle loading to 10 % fumed silica increases the dynamic yield stress by about an order of magnitude at room temperature with a steady state value of τ_f near 10^3 Pa. Heating to the cure temperature reveals a decrease in τ_f from the steady state values at room temperature, and this effect is exacerbated by higher temperatures and increased particle loadings. For the 5 % fumed silica filled resins, heating to 100 °C causes a 30 % decrease in τ_f while heating to the lower cure temperature leads to a negligible decrease in the yield stress. The decrease in τ_f is exacerbated for the 10 % fumed silica filled resins, which shows a 65 % to 70 % decrease at both cure temperatures. For the resin with 10 % fumed silica, there is only a small difference in the first yield stress measured at 70 °C and 100 °C. This could be the result of batch-to-batch variation in the resin, which leads to differences in the applied shear history. It could also be caused by the additional crosslinking experienced at the higher

temperature before measurements could be taken. Temperature was ramped at 10 °C/min for both tests, meaning that the material cured at 100 °C experienced 3 more minutes at elevated temperature before the first yield stress measurement.

The strong temperature dependence and nonmonotonic response of τ_f is due largely to the fact that the material is well outside the linear viscoelastic response range of the filled resin. Because the network structure must be ruptured to measure τ_f, the dynamic yield stress depends both on the structure of the broken fumed silica network and the properties of the curing resin that forms the matrix. The dramatic decrease in τ_f immediately after reaching the cure temperature is most likely due to a sharp decrease in the resin viscosity at higher temperatures, as shown by comparing G'' to G''_{RT} in Figure 3b and Figure 4a, as well as the steady shear measurements of Davis et al. [34]. Significant additional work is required to fully understand why filler content and temperature have the presented effects on the yield stress. Experiments that vary the recovery period would provide insight into the role of thixotropy in these types of tests. Varying filler size and shape may also reveal how these factors affect the yield stress evolution and thixotropy at elevated temperatures. However, these studies fall outside the scope of the current work and warrant their own dedicated study.

Figure 6 shows a selection of the stress sweeps used to generate Figure 5. Note that a dynamic yield stress is only reported in Figure 5 when a crossover in $G' - G''$ is observed; once τ_f exceeds the maximum applied stress for each particle loading (2000 Pa for 5 % fumed silica and 10000 Pa for 10 % fumed silica) the value is no longer reported, although we can assume that τ_f exceeds those stresses. Once at the cure temperature, τ_f initially increases, but the growth in τ_f depends strongly on both particle loading and cure temperature. In general, filled resins cured at 100 °C show a rapid increase in τ_f above the values measured at room temperature, and after 1000 s the dynamic yield stress exceeds the measurement range. Curing at 70 °C reveals a slower increase in τ_f with a local maximum in the dynamic yield stress near 2000 s for both filled resins. Figure 6a,b shows that at this point the loss modulus of the resin begins to grow much more quickly than the storage modulus. This behavior is so strong in the resin with 5 % fumed silica (Figure 6a) that at 2771 s, G'' overtakes G' at 80 Pa, even though there is no decrease is G'. In short, this crossover is believed to be caused by reaction kinetics rather than yielding and is therefore not believed to indicate reduced structural stability. Between the measurement at 2771 s and 4254 s, the stress sweeps were terminated at the first stress tested, because G'' was greater than G' (i.e., $\delta > 1$). At 4254 s, G' finally reaches a value greater than G'', however, the moduli do not crossover below the maximum stress tested (2000 Pa). Thus, τ_f is assumed to be greater than 2000 Pa after 4254 s.

Although the stress sweeps rupture the network structure of the composite resins, the additional stress does not appear to significantly affect the liquid to solid transition or the reaction kinetics. Figure S5 plots the conversion evolution during the stress sweep experiments (Figure 7d) over that of the SAOS experiments (Figure 3d) and shows that the stress sweep experiments do not significantly change the reaction kinetics. Further, the evolution of moduli measurements at the end of each recovery period (Figure 7a–c) matches

that of the SAOS tests presented in Figure 3a–c. However, the resins that experienced flow exhibit lower moduli and higher tan δ, which is to be expected after network rupture. When cured at 70 °C, the storage modulus also decreases slightly just before gelation (Figure 7a), indicating that the material does not achieve full recovery during the recovery period. This is only true immediately before the gel point and is expected because the loss modulus (as well as viscosity and relaxation time) increases rapidly immediately prior to gelation (Figure 7b and Figure S6). Longer recovery periods may allow for full recovery but would reduce the number of yield stress measurements in these quickly evolving resins.

We can gain a better understanding of the nonmonotonic response of τ_f via the conversion dependence shown in Figure 8. The room-temperature τ_f is represented by a shaded region labeled τ_f^{RT}, which corresponds to the final room-temperature dynamic yield stress measured before the isothermal cure. These results reveal that, unlike the storage and loss moduli shown in Figure 4, the dynamic yield stress depends on both cure temperature and particle loading. The samples cured at the lower temperature achieve $\tau_f > \tau_f^{RT}$ at a lower conversion compared to the filled resins cured at 100 °C, despite the significantly faster conversion kinetics at higher temperatures. The dynamic yield stress is also much more sensitive to conversion early in the cure process ($\alpha < 0.3$) than the linear viscoelastic properties – there is little change in G' or G'' in this conversion range in Figure 4. The maximum in τ_f for the samples cured at 70 °C occurs near $\alpha = 0.4$, which (according to Figure 4a) is also where G'' begins to significantly increase in the filled resins. This indicates that the viscous response of the particle network is an important contribution to the dynamic yield stresses measured here. Values of τ_f exceed the measurement threshold at or below a conversion of 0.7 independent of temperature and particle loading, indicating that the dynamic yield stress sharply increases when a chemically crosslinked network is formed in the resin.

The dynamic yield stress measurements reveal a strong temperature and conversion sensitivity that is not evident in the SAOS results. These results again highlight the sensitivity of the nonlinear regime to changes in structure and morphology. In addition, the results shown in Figure 8 suggest simple processing strategies to mitigate detrimental changes in material properties, which will be discussed in the following section.

Stress sweeps on the filled resins without curing agent, in Figure 9, illustrate the effects of temperature in the absence of crosslinking. The linear viscoelastic storage modulus (Figure 9a,c) of the uncured material is more sensitive to temperature than indicated by Figure 3a. This finding suggests that small amounts of crosslinking contribute to the storage modulus, making it insensitive to temperature early in the cure. Figure 9a,c also show that the dynamic yield stress is highly dependent on temperature for both filled resins. For the resin with 5 % fumed silica, the yield stress drops from 217 Pa at room temperature to 70 Pa at 100 °C. Likewise, the resin with 10 % fumed silica drops from 1575 Pa at room temperature to 461 Pa at 100 °C. This finding suggests that the drop in yield stress observed in Figure 5 cannot be solely attributed to thixotropic effects and does represent the temperature sensitivity of the yield stress. The normalized recovered storage modulus (i.e., the storage modulus during recovery divided by the storage modulus in the linear viscoelastic regime from the stress sweeps in Figure 9a,c) is presented in Figure 9b,d. For both resins at room temperature,

the storage modulus only recovers to between 70 % and 75 % of its original value after 900 s (i.e., 15 min). At 100 °C, both resins exceed 85 % recovery after 120 s (the recovery time used in experiments) and virtually fully recover after 900 s. This means that the thixotropic timescale is longer than 900 s at room temperature but becomes much shorter at elevated temperature. This finding further suggests that the thixotropic effects are small at elevated temperatures and the drop in yield stress can be primarily attributed to temperature sensitivity.

3.4 Application

The rheology-conversion results shown in Figure 4 and Figure 8 motivate a two-step cure schedule that mitigates the drop in dynamic yield stress during curing and achieves a high conversion. Here, we focus on the 5 % fumed silica filled resin which shows a negligible decrease in the dynamic yield stress upon heating to 70 °C but vitrifies at later times. The results from Figure 8 were used to determine the conversion at which the dynamic yield stress exceeds τ_f^{RT} at 100 °C, which occurs at a conversion of approximately 0.36. Therefore, a two-step cure process where the filled resin is first cured at the lower cure temperature, then post-cured at the higher cure temperature once the conversion exceeds 0.36 should avoid detrimental losses in material properties while increasing the final conversion.

Figure 10 compares the two-step cure with the previously presented isothermal results for the 5 % fumed silica filled resin. Figure 10a shows that the dynamic yield stress in the first step of the two-step cure follows that of the isothermal cure at 70 °C with a negligible decrease from the room-temperature value. After ramping to 100 °C, the dynamic yield stress remains above τ_f^{RT}. This result suggests that the two-step cure improves structural stability compared to an isothermal cure at 100 °C. Figure 10b shows that during the first step, the two-step cure reacts at the same rate as the 70 °C isothermal cure. After ramping to 100 °C, the reaction accelerates and reaches a greater final conversion than the isothermal cure at 70 °C, illustrating two key benefits of the two-step cure. The material cured isothermally at 70 °C reaches a maximum conversion around 0.9 in about 12500 s, whereas the two-step cure reaches the same level of conversion in only 4000 s. The two-step cure takes less than a third of the time, saving more than 2 hours. Figure 10c shows that the two-step cure avoids the vitrification peak of the isothermal cure at 70 °C that halts the reaction. This explains why the two-step cure achieved greater conversion than the isothermal cure at 70 °C. Finally, Figure 10d shows that the storage modulus of the two-step cure mirrors behavior at both temperatures until the curves diverge due to vitrification, where the two-step cure follows behavior at 100 °C.

Previous research in ultraviolet dual-cure systems and filament winding processes [20, 21, 23, 36, 59, 100–102] suggests that drops in the viscoelastic properties can be mitigated if the material has chemically gelled and formed a network before ramping to an elevated temperature. We note that the conversion where the temperature can be increased in the two-step procedure ($\alpha \approx 0.36$) is well below the critical chemical gel point of approximately 0.7. Compared to a profile that increases cure temperature at the gel point, the presented two-step cure spends significantly less time at the lower cure temperature, which reduces the overall time necessary to drive the cure to completion. Figure 10b shows that it takes around

4200 s for the 70 °C cure to reach $\alpha \approx 0.7$, whereas the two-step cure only takes about 2400 s to reach the same conversion. Therefore, ramping to 100 °C at $\alpha \approx 0.36$ rather than 0.7 saves approximately 1800 s (0.5 h).

To test the two-step cure profile in a more conventional curing system, we cure samples of the 5 % fumed silica filled resin in an oven (Fisherbrand Isotemp Model 281A Vacuum Oven, Fisher Scientific, Massachusetts, USA) using the two-step cure and under isothermal conditions at 70 °C and 100 °C. The ramp rate of the oven (approximately 2.5 °C/min) is slower than that applied by the rheometer (10 °C/min). All samples are allowed to cure for a total of 3 h to enable comparison of their final conversion measured via Raman spectroscopy (Figure 11). Therefore, the two-step cure samples were held for approximately 25 min at 70 °C until the conversion was expected to exceed 0.36 (according to Figure 8), then ramped to 100 °C over the course of 12 min, then post-cured for 143 min at 100 °C. As expected, the 70 °C samples reached the lowest average conversion, whereas the 100 °C samples reached the highest average conversion. Confirming one of the key benefits of using the two-step cure, the average conversion of the two-step samples exceeded that of the 70 °C samples by 0.07. Conversely, the average conversion of the two-step cure fell 0.03 below that of the 100 °C cure, which is most likely due to spending less time at 100 °C than the isothermally cured sample. However, it is encouraging that the two-step cure results in conversion near the isothermal 100 °C cure and well above the conversion of the 70 °C sample. These strategies reduce the overall time and energy required to generate samples with a high degree of cure without sacrificing rheological properties during cure.

4 Discussion

These results show that simultaneous characterization of rheological properties and conversion can provide critical insight into the key factors governing mechanical stability during curing, which have direct implications for curing freestanding structures in processes like material extrusion. This understanding enables the design of curing schedules that mitigate drops in properties associated with the structural stability of printed parts with minimal reductions in curing speed and final conversion. The effects of temperature and conversion on the minimum rheological properties suggest that thermal post-curing is the limiting factor that determines the scale at which thermally post-cured material extrusion is no longer feasible and in-process curing becomes necessary. While the present work does not demonstrate the effects of tailored curing schedules on structural stability of printed parts, it motivates and lays the groundwork for such experiments.

Here, we show that the uncured storage modulus increases when more filler is added, resulting in filled resins that are more resistant to self-weight buckling [57]. Increasing temperature does not appear to affect the storage modulus early in the cure (Figure 4b), suggesting that stable printed parts are not likely to buckle during post-curing. However, the storage modulus decreases slightly during the ramp to the isothermal temperature (Figure S7). These minor decreases are inconsequential in the context of structural stability because self-weight buckling scales with $(G')^{1/3}$ [57]. The decreasing storage modulus plateaus when the ramp exceeds approximately 50 °C. This behavior makes these composite resins resistant to self-weight buckling during curing, providing little opportunity to tailor curing schedules

to mitigate collapse. On the other hand, the dynamic yield stress is highly dependent on temperature early in the cure. Since self-weight yielding scales linearly with the yield stress, a reduction in the yield stress of 30 % corresponds to a 30 % reduction in the height that can be sustained during thermal post-curing. Therefore, the relatively large decrease in yield stress suggests that self-weight yielding is more likely to cause collapse while curing than self-weight buckling [57, 58]. Increasing filler content increases the dynamic yield stress at room temperature, improving structural stability during the printing process at the cost of flow processability. However, the decrease in dynamic yield stress at elevated temperatures becomes more pronounced as filler content increases. Thus, increasing filler content does not improve structural stability during thermal post-curing as much as the room-temperature dynamic yield stress indicates.

Our choice to measure the dynamic yield stress is motivated by the short measurement duration relative to the rate at which rheological properties evolve during crosslinking. However, the dynamic yield stress typically exceeds the stress at which the material stops behaving elastically [99], potentially overestimating the material property that governs stability in predictive models for material extrusion [57, 58]. An additional challenge is that testing the dynamic yield stress necessarily destroys the microstructure that gives rise to the material properties of interest. The recovery period between stress amplitude sweeps allows for some re-formation of structure, but as the matrix resin approaches the critical gel, the viscosity increases dramatically, and the timescales required for equilibration must therefore also increase. Despite these limitations, the dynamic yield stress results for the two-step cure process demonstrate that a tailored cure schedule developed from straightforward rheo-Raman measurements can be used to avoid potentially detrimental reductions in rheological properties. Epoxy-amine chemistry is well-developed with tunable reaction kinetics, and a resin that cures more slowly while avoiding vitrification would allow for various yield stress measurements and additional time for structural recovery. Such work warrants its own dedicated study and is not addressed here.

Multi-step cure profiles are common in thermoset composite resins and are often premised on forming a crosslinked network to hold the material in place before stepping up to a higher temperature [13, 20–24, 36, 59, 100–102]. However, these rheo-Raman measurements demonstrate that the cure step can be performed well before critical gelation occurs, which decreases the time required to cure these composite materials. We show that the dynamic yield stress exceeds its room-temperature value well before critical gelation, indicating that the material becomes protected from self-weight yielding before the gel point. The resulting two-step cure profile is faster than a profile based on the gel point and still allows us to avoid reductions in the rheological properties linked to structural instability without increasing filler loading, which has been shown to be less effective than room-temperature measurements indicate. Multi-step cure processing therefore offers an efficient method to widen the composition and mechanical property space for filled thermoset resins used in processes like thermally post-cured material extrusion. The success of this method builds a foundation for future work that utilizes Raman capabilities to govern a feedback loop that controls oven temperature to maintain structural stability and maximize curing speed of printed parts. The optimal cure schedule also represents the limit at which thermally post-cured material extrusion can produce stable structures for a given filler loading.

5 Conclusion

Simultaneous measurements of rheology and Raman spectroscopy allow for direct correlation between chemical crosslinking and the rheological properties that govern structural stability, namely the storage modulus and yield stress. Early in the cure, the storage modulus is sensitive to particle loading but not temperature, and rheo-Raman measurements highlight the sensitivity of the modulus of filled resins to conversion near gelation and vitrification of the resin matrix. Measurements of the dynamic yield stress based on the $G' - G''$ crossover reveal sensitivity to particle loading, temperature, and conversion well below the gel point. Simultaneous characterization of the dynamic yield stress and conversion enable the design of a curing schedule that eliminates the decrease in dynamic yield stress while quickly driving the reaction to high conversion. Notably, the two-step approach used here does not require gelation prior to the higher temperature post-cure, enabling a more efficient curing process than indicated by previous thermoset composite research. This approach provides an alternative to increasing filler content to improve structural stability, which hinders flow processability, reduces control over final properties, and is less effective than room-temperature measurements indicate. These findings help to understand the scale at which thermally post-cured material extrusion is no longer feasible and when in-process curing becomes necessary.

The systematic rheo-Raman evaluation of properties at different temperatures and filler contents presented here builds a strong foundation for future work on thermosetting materials. Studying the effects of different fillers, epoxies, or amines on the evolution of properties would broaden understanding of how material formulation affects stability during post-curing. Additionally, multi-frequency testing would provide more accurate gel point measurements and better understanding of how rheological properties evolve in relation to the gel point. Future work could also focus on rheo-Raman analysis at more temperatures, which could enable the design of curing schedules that minimize curing time by incorporating more than just two isothermal steps. These results could be applied to use in situ Raman monitoring to control oven temperature during curing and maximize processing speed. Finally, one of the most important next steps for the additive manufacturing community is to print and cure parts to confirm that the conclusions made from the rheo-Raman findings agree with observed structural stability.

Supplementary Material

Refer to Web version on PubMed Central for supplementary material.

Acknowledgements

SKR would like to thank Jeremiah Woodcock and Jonathan Seppala for generously sharing equipment, facilities, and knowledge.

References

[1]. Compton BG, Lewis JA, 3D-Printing of Lightweight Cellular Composites, Adv. Mater. 26(34) (2014) 5930–5935. 10.1002/adma.201401804. [PubMed: 24942232]

[2]. Duoss EB, Weisgraber TH, Hearon K, Zhu C, Small IV W, Metz TR, Vericella JJ, Barth HD, Kuntz JD, Maxwell RS, Spadaccini CM, Wilson TS, Three-Dimensional Printing of Elastomeric, Cellular Architectures with Negative Stiffness, Adv. Funct. Mater. 24(31) (2014) 4905–4913. 10.1002/adfm.201400451.

[3]. Raney JR, Compton BG, Mueller J, Ober TJ, Shea K, Lewis JA, Rotational 3D printing of damage-tolerant composites with programmable mechanics, Proc. Natl. Acad. Sci. U. S. A. 115(6) (2018) 1198–1203. 10.1073/pnas.1715157115. [PubMed: 29348206]

[4]. Mueller J, Raney JR, Shea K, Lewis JA, 2018. Architected Lattices with High Stiffness and Toughness via Multicore–Shell 3D Printing, Adv. Mater. 30(12), 1705001. 10.1002/adma.201705001.

[5]. Hmeidat NS, Kemp JW, Compton BG, High-strength epoxy nanocomposites for 3D printing, Compos. Sci. Technol. 160 (2018) 9–20. 10.1016/j.compscitech.2018.03.008.

[6]. Chandrasekaran S, Duoss EB, Worsley MA, Lewicki JP, 3D printing of high performance cyanate ester thermoset polymers, J. Mater. Chem. A 6(3) (2018) 853–858. 10.1039/C7TA09466C.

[7]. Johnson KJ, Wiegart L, Abbott AC, Johnson EB, Baur JW, Koerner H, In Operando Monitoring of Dynamic Recovery in 3D-Printed Thermoset Nanocomposites by XPCS, Langmuir 35(26) (2019) 8758–8768. 10.1021/acs.langmuir.9b00766. [PubMed: 31244252]

[8]. Pack RC, Romberg SK, Badran AA, Hmeidat NS, Yount T, Compton BG, 2020. Carbon Fiber and Syntactic Foam Hybrid Materials via Core–Shell Material Extrusion Additive Manufacturing, Adv. Mater. Technol. 5(12), 2000731. 10.1002/admt.202000731.

[9]. Johnson MV, Garanger K, Hardin JO, Berrigan JD, Feron E, Kalidindi SR, 2021. A generalizable artificial intelligence tool for identification and correction of self-supporting structures in additive manufacturing processes, Addit. Manuf. 46, 102191. 10.1016/j.addma.2021.102191.

[10]. Kemp JW, Diaz AA, Malek EC, Croom BP, Apostolov ZD, Kalidindi SR, Compton BG, Rueschhoff LM, 2021. Direct ink writing of ZrB2-SiC chopped fiber ceramic composites, Addit. Manuf. 44, 102049. 10.1016/j.addma.2021.102049.

[11]. Wright WJ, Darville J, Celik N, Koerner H, Celik E, 2022. In-situ optimization of thermoset composite additive manufacturing via deep learning and computer vision, Addit. Manuf. 58, 102985. 10.1016/j.addma.2022.102985.

[12]. Trigg EB, Hmeidat NS, Smieska LM, Woll AR, Compton BG, Koerner H, 2021. Revealing filler morphology in 3D-printed thermoset nanocomposites by scanning microbeam X-ray scattering, Addit. Manuf. 37, 101729. 10.1016/j.addma.2020.101729.

[13]. Calvert P, Lin TL, Martin H, Extrusion Freeform Fabrication of Chopped-Fibre Reinforced Composites, High Perform. Polym. 9(4) (1997) 449–456. 10.1088/0954-0083/9/4/008.

[14]. Crowley AG, Tran TQ, Green MJ, Using nanomaterials to enhance the additive manufacturing of polymeric resins, Nano Futures 6(4) (2022) 042502. 10.1088/2399-1984/aca130.

[15]. Wilt JK, Gilmer D, Kim S, Compton BG, Saito T, Direct ink writing techniques for in situ gelation and solidification, MRS. Commun. 11(2) (2021) 106–121. 10.1557/s43579-020-00006-8.

[16]. Gao C, Qiu J, Wang S, 2022. In-situ curing of 3D printed freestanding thermosets, J. Adv. Manuf. Process. 4(3), e10114. 10.1002/amp2.10114.

[17]. Xu X, Yang J, Jonhson W, Wang Y, Suwardi A, Ding J, Guan C, Zhang D, 2022. Additive manufacturing solidification methodologies for ink formulation, Addit. Manuf. 56, 102939. 10.1016/j.addma.2022.102939.

[18]. Lebel LL, Aissa B, Khakani MAE, Therriault D, Ultraviolet-Assisted Direct-Write Fabrication of Carbon Nanotube/Polymer Nanocomposite Microcoils, Adv. Mater. 22(5) (2010) 592–596. 10.1002/adma.200902192. [PubMed: 20217755]

[19]. Kokkinis D, Schaffner M, Studart AR, 2015. Multimaterial magnetically assisted 3D printing of composite materials, Nat. Commun. 6(1), 8643. 10.1038/ncomms9643. [PubMed: 26494528]

[20]. Griffini G, Invernizzi M, Levi M, Natale G, Postiglione G, Turri S, 3D-printable CFR polymer composites with dual-cure sequential IPNs, Polymer 91 (2016) 174–179. 10.1016/j.polymer.2016.03.048.

[21]. Wu T, Jiang P, Zhang X, Guo Y, Ji Z, Jia X, Wang X, Zhou F, Liu W, 2019. Additively manufacturing high-performance bismaleimide architectures with ultraviolet-assisted direct ink writing, Mater. Des. 180, 107947. 10.1016/j.matdes.2019.107947.

[22]. Armstrong CD, Yue L, Demoly F, Zhou K, Qi HJ, 2023. Unstructured Direct Ink Write 3D Printing of Functional Structures with Ambient Temperature Curing Dual-Network Thermoset Ink, Advanced Intelligent Systems 5(1), 2200226. 10.1002/aisy.202200226.

[23]. Kopatz JW, Unangst J, Cook AW, Appelhans LN, 2021. Compositional effects on cure kinetics, mechanical properties and printability of dual-cure epoxy/acrylate resins for DIW additive manufacturing, Addit. Manuf. 46, 102159. 10.1016/j.addma.2021.102159.

[24]. Tu R, Sodano HA, 2021. Additive manufacturing of high-performance vinyl ester resin via direct ink writing with UV-thermal dual curing, Addit. Manuf. 46, 102180. 10.1016/j.addma.2021.102180.

[25]. Stiles A, Tison T-A, Pruitt L, Vaidya U, 2022. Photoinitiator Selection and Concentration in Photopolymer Formulations towards Large-Format Additive Manufacturing, Polymers 14(13), 2708. 10.3390/polym14132708. [PubMed: 35808752]

[26]. Rios O, Carter W, Post B, Lloyd P, Fenn D, Kutchko C, Rock R, Olson K, Compton B, 3D printing via ambient reactive extrusion, Mater. Today Commun. 15 (2018) 333–336. 10.1016/j.mtcomm.2018.02.031.

[27]. Walker S, Daalkhaijav U, Thrush D, Branyan C, Yirmibesoglu OD, Olson G, Menguc Y, Zero-Support 3D Printing of Thermoset Silicone Via Simultaneous Control of Both Reaction Kinetics and Transient Rheology, 3D Print. Addit. Manuf. 6(3) (2019) 139–147. 10.1089/3dp.2018.0117.

[28]. Romberg SK, Hershey CJ, Lindahl JM, Carter WG, Condon J, Kunc V, Compton BG, Large-scale reactive thermoset printing: Complex interactions between temperature evolution, viscosity, and cure shrinkage, Int. J. Adv. Manuf. Technol. 123(9) (2022) 3079–3094. 10.1007/s00170-022-10380-3.

[29]. Robertson ID, Yourdkhani M, Centellas PJ, Aw JE, Ivanoff DG, Goli E, Lloyd EM, Dean LM, Sottos NR, Geubelle PH, Moore JS, White SR, Rapid energy-efficient manufacturing of polymers and composites via frontal polymerization, Nature 557(7704) (2018) 223–227. 10.1038/s41586-018-0054-x. [PubMed: 29743687]

[30]. Uitz O, Koirala P, Tehrani M, Seepersad CC, 2021. Fast, low-energy additive manufacturing of isotropic parts via reactive extrusion, Addit. Manuf. 41, 101919. 10.1016/j.addma.2021.101919.

[31]. Odom MGB, Sweeney CB, Parviz D, Sill LP, Saed MA, Green MJ, Rapid curing and additive manufacturing of thermoset systems using scanning microwave heating of carbon nanotube/epoxy composites, Carbon 120 (2017) 447–453. 10.1016/j.carbon.2017.05.063.

[32]. Sarmah A, Desai SK, Crowley AG, Zolton GC, Tezel GB, Harkin EM, Tran TQ, Arole K, Green MJ, Additive manufacturing of nanotube-loaded thermosets via direct ink writing and radio-frequency heating and curing, Carbon 200 (2022) 307–316. 10.1016/j.carbon.2022.08.063.

[33]. Sun Y, Wang L, Ni Y, Zhang H, Cui X, Li J, Zhu Y, Liu J, Zhang S, Chen Y, Li M, 2023. 3D printing of thermosets with diverse rheological and functional applicabilities, Nat. Commun. 14(1), 245. 10.1038/s41467-023-35929-y. [PubMed: 36646723]

[34]. Davis CS, Orloff ND, Woodcock JW, Long CJ, Twedt KA, Natarajan B, Seppala JE, McClelland JJ, Obrzut J, Liddle JA, Gilman JW, Cure temperature influences composite electrical properties by carbon nanotube-rich domain formation, Compos. Sci. Technol. 133 (2016) 23–32. 10.1016/j.compscitech.2016.07.012.

[35]. Garschke C, Parlevliet PP, Weimer C, Fox BL, Cure kinetics and viscosity modelling of a high-performance epoxy resin film, Polym. Test. 32(1) (2013) 150–157. 10.1016/j.polymertesting.2012.09.011.

[36]. Faria H, Analytical and Numerical Modelling of the Filament Winding Process, Faculdade de Engenharia Universidade Do Porto, 2013, p. 262.

[37]. Castro JM, Macosko C, Kinetics and rheology of typical polyurethane reaction injection molding systems, SPE ANTEC 1980, 1980.

[38]. Macosko C, RIM Fundamentals of Reaction Injection Molding, Hanser, Munich, 1989.

[39]. Wimmer MG, Compton BG, 2022. Semi-solid epoxy feedstocks with high glass transition temperature for material extrusion additive manufacturing, Addit. Manuf. 54, 102725. 10.1016/j.addma.2022.102725.

[40]. Carrola M, Asadi A, Zhang H, Papageorgiou DG, Bilotti E, Koerner H, 2021. Best of Both Worlds: Synergistically Derived Material Properties via Additive Manufacturing of Nanocomposites, Adv. Funct. Mater. 31(46), 2103334. 10.1002/adfm.202103334.

[41]. Chen Q, Han L, Ren J, Rong L, Cao P, Advincula RC, 4D Printing via an Unconventional Fused Deposition Modeling Route to High-Performance Thermosets, ACS Appl. Mater. Interfaces 12(44) (2020) 50052–50060. 10.1021/acsami.0c13976. [PubMed: 33103879]

[42]. Chike KE, Myrick ML, Lyon RE, Raman and Near-Infrared Studies of an Epoxy Resin, Appl. Spectrosc. 47(10) (1993) 1631–1635. 10.1366/0003702934334714.

[43]. Lyon RE, Chike KE, Angel SM, In situ cure monitoring of epoxy resins using fiber-optic Raman spectroscopy, J. Appl. Polym. Sci. 53(13) (1994) 1805–1812. 10.1002/app.1994.070531310.

[44]. Benali S, Bouchet J, Lachenal G, Chemeorheology: A New Design for Simultaneous Rheological and Fourier Transform near Infrared Analysis, J. Near Infrared Spectrosc. 12(1) (2004) 5–13. 10.1255/jnirs.403.

[45]. Botella A, Dupuy J, Roche A-A, Sautereau H, Verney V, Photo-Rheometry/NIR Spectrometry: An in situ Technique for Monitoring Conversion and Viscoelastic Properties during Photopolymerization, Macromol. Rapid Commun. 25(12) (2004) 1155–1158. 10.1002/marc.200400087.

[46]. Schmidt C, Scherzer T, Monitoring of the shrinkage during the photopolymerization of acrylates using hyphenated photorheometry/near-infrared spectroscopy, J. Polym. Sci. B Polym. Phys. 53(10) (2015) 729–739. 10.1002/polb.23694.

[47]. Fu X.-l., Fan X.-z., Curing reaction kinetics of HTPE polymer studied by simultaneous rheometry and FTIR measurements, J. Therm. Anal. Calorim. 125(2) (2016) 977–982. 10.1007/s10973-016-5485-8.

[48]. Steeman PAM, Dias AA, Wienke D, Zwartkruis T, Polymerization and Network Formation of UV-Curable Systems Monitored by Hyphenated Real-Time Dynamic Mechanical Analysis and Near-Infrared Spectroscopy, Macromolecules 37(18) (2004) 7001–7007. 10.1021/ma049366c.

[49]. Gorsche C, Harikrishna R, Baudis S, Knaack P, Husar B, Laeuger J, Hoffmann H, Liska R, Real Time-NIR/MIR-Photorheology: A Versatile Tool for the in Situ Characterization of Photopolymerization Reactions, Anal. Chem. 89(9) (2017) 4958–4968. 10.1021/acs.analchem.7b00272. [PubMed: 28383904]

[50]. Marotta A, Faggio N, Ambrogi V, Cerruti P, Gentile G, Mija A, Curing Behavior and Properties of Sustainable Furan-Based Epoxy/Anhydride Resins, Biomacromolecules 20(10) (2019) 3831–3841. 10.1021/acs.biomac.9b00919. [PubMed: 31412201]

[51]. Radebe NW, Fengler C, Klein CO, Figuli R, Wilhelm M, Rheo-IR: A combined setup for correlating chemical changes via FTIR spectroscopy and rheological properties in a strain-controlled rheometer, J. Rheol. 65(4) (2021) 681–693. 10.1122/8.0000251.

[52]. Farquharson S, Carignan J, Khitrov V, Senador A, Shaw M, Development of a phase diagram to control composite manufacturing using Raman spectroscopy, Optical Technologies for Industrial, Environmental, and Biological Sensing, SPIE, 2004. 10.1117/12.512227.

[53]. Chevrel M-C, Hoppe S, Falk L, Nadège B, Chapron D, Bourson P, Durand A, Rheo-Raman: A Promising Technique for In Situ Monitoring of Polymerization Reactions in Solution, Ind. Eng. Chem. Res. 51(49) (2012) 16151–16156. 10.1021/ie302054k.

[54]. Kotula AP, Meyer MW, Vito FD, Plog J, Walker ARH, Migler KB, 2016. The rheo-Raman microscope: Simultaneous chemical, conformational, mechanical, and microstructural measures of soft materials, Rev. Sci. Instrum. 87(10), 105105. 10.1063/1.4963746. [PubMed: 27802720]

[55]. Strobel ME, Set up of an online rheo-Raman system to measure the crosslinking of polymers, Johannes Kepler Universitat Linz, 2019, p. 103.

[56]. Kotula AP, Woodcock JW, Gilman JW, Holmes GA, Reaction-Induced Phase Separation (RIPS) in Amine-Cured Epoxy/Epoxy Thermosets. 3. A Cure Kinetics Investigation by Rheo-Raman Spectroscopy, Polymer (Submitted).

[57]. Romberg SK, Islam MA, Hershey CJ, DeVinney M, Duty CE, Kunc V, Compton BG, 2021. Linking thermoset ink rheology to the stability of 3D-printed structures, Addit. Manuf. 37, 101621. 10.1016/j.addma.2020.101621.

[58]. Romberg SK, Abir AI, Hershey CJ, Kunc V, Compton BG, 2022. Structural stability of thin overhanging walls during material extrusion additive manufacturing of thermoset-based ink, Addit. Manuf. 53, 102677. 10.1016/j.addma.2022.102677.

[59]. Invernizzi M, Natale G, Levi M, Turri S, Griffini G, 2016. UV-Assisted 3D Printing of Glass and Carbon Fiber-Reinforced Dual-Cure Polymer Composites, Mater. 9(7), 583. 10.3390/ma9070583.

[60]. Cassagnau P, Melt rheology of organoclay and fumed silica nanocomposites, Polymer 49(9) (2008) 2183–2196. 10.1016/j.polymer.2007.12.035.

[61]. Barthel H, Surface interactions of dimethylsiloxy group-modified fumed silica, Colloids surf. A Physiochem. eng. Asp. 101(2) (1995) 217–226. 10.1016/0927-7757(95)03179-H.

[62]. Chiou B-S, Raghavan SR, Khan SA, Effect of Colloidal Fillers on the Cross-Linking of a UV-Curable Polymer: Gel Point Rheology and the Winter−Chambon Criterion, Macromolecules 34(13) (2001) 4526–4533. 10.1021/ma010281a.

[63]. Barthel H, Dreyer M, Gottschalk-Gaudig T, Litvinov V, Nikitina E, Fumed silica – rheological additive for adhesives, resins, and paints, Macromol. Symp. 187(1) (2002) 573–584. 10.1002/1521-3900(200209)187:1<573::AID-MASY573>3.0.CO;2-1.

[64]. Kawaguchi M, Dispersion stabilities and rheological properties of fumed silica suspensions, J. Disperse Sci. Technol. 38(5) (2017) 642–660. 10.1080/01932691.2016.1185952.

[65]. Huang GC, Lee JK, Isothermal cure characterization of fumed silica/epoxy nanocomposites: The glass transition temperature and conversion, Compos. Part A Appl. Sci. Manuf. 41(4) (2010) 473–479. 10.1016/j.compositesa.2009.12.003.

[66]. Ettlinger M, Ladwig T, Weise A, Surface modified fumed silicas for modern coatings, Prog. Org. Coat. 40(1) (2000) 31–34. 10.1016/S0300-9440(00)00151-X.

[67]. Whitby CP, Krebsz M, Booty SJ, Understanding the role of hydrogen bonding in the aggregation of fumed silica particles in triglyceride solvents, J. Colloid Interface Sci. 527 (2018) 1–9. 10.1016/j.jcis.2018.05.029. [PubMed: 29775816]

[68]. Wu W.-l., Bauer BJ, Epoxy network structure. 3. Neutron-scattering study of epoxies containing monomers of different molecular weight, Macromolecules 19(6) (1986) 1613–1618. 10.1021/ma00160a021.

[69]. Lee A, McKenna GB, Effect of crosslink density on physical ageing of epoxy networks, Polymer 29(10) (1988) 1812–1817. 10.1016/0032-3861(88)90396-5.

[70]. G'Sell C, McKenna GB, Influence of physical ageing on the yield response of model DGEBA/poly(propylene oxide) epoxy glasses, Polymer 33(10) (1992) 2103–2113. 10.1016/0032-3861(92)90876-X.

[71]. Huang ML, Williams JG, Mechanisms of Solidification of Epoxy-Amine Resins During Cure, Macromolecules 27(25) (1994) 7423–7428. 10.1021/ma00103a026.

[72]. Landry CJT, Coltrain BK, Landry MR, Fitzgerald JJ, Long VK, Poly(vinyl acetate)/silica-filled materials: material properties of in situ vs fumed silica particles, Macromolecules 26(14) (1993) 3702–3712. 10.1021/ma00066a032.

[73]. Zhong X, Liu Y, Su H, Zhan G, Yu Y, Gan W, Enhanced viscoelastic effect of mesoscopic fillers in phase separation, Soft Matter 7(7) (2011) 3642–3650. 10.1039/C0SM01445A.

[74]. Zhang J, Li T, Hu Z, Wang H, Yu Y, Effect of size and content of mesoscopic fillers on the polymerization induced viscoelastic phase separation, RSC Adv. 4(1) (2014) 442–454. 10.1039/C3RA44536D.

[75]. Chae G-S, Park H-W, Kwon K, Shin S, 2021. Comparative Study of the Impact Wedge-Peel Performance of Epoxy Structural Adhesives Modified with Functionalized Silica Nanoparticles, Polymers 13(3), 469. 10.3390/polym13030469. [PubMed: 33540714]

[76]. Hmeidat NS, Pack RC, Talley SJ, Moore RB, Compton BG, 2020. Mechanical anisotropy in polymer composites produced by material extrusion additive manufacturing, Addit. Manuf. 34, 101385. 10.1016/j.addma.2020.101385.

[77]. Friedrich LM, Gunther RT, Seppala JE, Suppression of Filament Defects in Embedded 3D Printing, ACS Appl. Mater. Interfaces 14(28) (2022) 32561–32578. 10.1021/acsami.2c08047. [PubMed: 35786823]

[78]. Schröter K, Hutcheson SA, Shi X, Mandanici A, McKenna GB, 2006. Dynamic shear modulus of glycerol: Corrections due to instrument compliance, J. Chem. Phys. 125(21), 214507. 10.1063/1.2400862. [PubMed: 17166033]

[79]. Romberg SK, Kotula AP, Simultaneous rheology and cure kinetics dictate thermal post-curing of thermoset composite resins, in: Repository NPD (Ed.) 2023. 10.18434/mds2-2918.

[80]. Zhang Z-M, Chen S, Liang Y-Z, Baseline correction using adaptive iteratively reweighted penalized least squares, Analyst 135(15) (2010) 1138–1146. 10.1039/B922045C. [PubMed: 20419267]

[81]. Hardis R, Jessop JLP, Peters FE, Kessler MR, Cure kinetics characterization and monitoring of an epoxy resin using DSC, Raman spectroscopy, and DEA, Compos. Part A Appl. Sci. Manuf. 49 (2013) 100–108. 10.1016/j.compositesa.2013.01.021.

[82]. Socrates G, Infrared and Raman characteristic group frequencies: tables and charts, John Wiley & Sons, Chichester, 2004.

[83]. Winter HH, Chambon F, Analysis of Linear Viscoelasticity of a Crosslinking Polymer at the Gel Point, J. Rheol. 30(2) (1986) 367–382. 10.1122/1.549853.

[84]. Winter HH, Can the gel point of a cross-linking polymer be detected by the $G' - G''$ crossover?, Polym. Eng. Sci. 27(22) (1987) 1698–1702. 10.1002/pen.760272209.

[85]. Chambon F, Winter HH, Linear Viscoelasticity at the Gel Point of a Crosslinking PDMS with Imbalanced Stoichiometry, J. Rheol. 31(8) (1987) 683–697. 10.1122/1.549955.

[86]. Winter HH, Mours M, Rheology of Polymers Near Liquid-Solid Transitions, Neutron Spin Echo Spectroscopy Viscoelasticity Rheology, Springer Berlin Heidelberg, Berlin, Heidelberg, 1997, pp. 165–234.

[87]. Geri M, Keshavarz B, Divoux T, Clasen C, Curtis DJ, McKinley GH, 2018. Time-Resolved Mechanical Spectroscopy of Soft Materials via Optimally Windowed Chirps, Phys. Rev. X 8(4), 041042. 10.1103/PhysRevX.8.041042.

[88]. Suman K, Joshi YM, On the universality of the scaling relations during sol-gel transition, J. Rheol. 64(4) (2020) 863–877. 10.1122/1.5134115.

[89]. Mewis J, Wagner NJ, Colloidal Suspension Rheology, Cambridge University Press, Cambridge, 2011.

[90]. Becker O, Simon GP, Varley RJ, Halley PJ, Layered silicate nanocomposites based on various high-functionality epoxy resins: The influence of an organoclay on resin cure, Polym. Eng. Sci. 43(4) (2003) 850–862. 10.1002/pen.10070.

[91]. Hayaty M, Beheshty MH, Esfandeh M, A new approach for determination of gel time of a glass/epoxy prepreg, J. Appl. Polym. Sci. 120(3) (2011) 1483–1489. 10.1002/app.33251.

[92]. Nohales A, López D, Culebras M, Gómez CM, Rheological study of gel phenomena during epoxide network formation in the presence of sepiolite, Polym. Int. 62(3) (2013) 397–405. 10.1002/pi.4321.

[93]. Burroughs MC, Schloemer TH, Congreve DN, Mai DJ, Gelation Dynamics during Photo-Cross-Linking of Polymer Nanocomposite Hydrogels, ACS Polymers Au (2022). 10.1021/acspolymersau.2c00051.

[94]. Enns JB, Gillham JK, Time–temperature–transformation (TTT) cure diagram: Modeling the cure behavior of thermosets, J. Appl. Polym. Sci. 28(8) (1983) 2567–2591. 10.1002/app.1983.070280810.

[95]. Tanaka Y, Stanford JL, Stepto R, Interpretation of Gel Points of an Epoxy-Amine System Including Ring Formation and Unequal Reactivity: Measurements of Gel Points and Analyses on Ring Structures, Macromolecules 45(17) (2012) 7197–7205. 10.1021/ma3009838.

[96]. Vidil T, Tournilhac F, Musso S, Robisson A, Leibler L, Control of reactions and network structures of epoxy thermosets, Prog. Polym. Sci. 62 (2016) 126–179. 10.1016/j.progpolymsci.2016.06.003.

[97]. Hiemenz PC, Lodge TP, Polymer Chemistry, 2 ed., CRC Press, Boca Raton, 2007.

[98]. Mours M, Winter HH, Time-resolved rheometry, Rheol. Acta 33(5) (1994) 385–397. 10.1007/BF00366581.

[99]. Dinkgreve M, Paredes J, Denn MM, Bonn D, On different ways of measuring “the” yield stress, J. Nonnewton Fluid Mech. 238 (2016) 233–241. 10.1016/j.jnnfm.2016.11.001.

[100]. Banerjee A, Sun L, Mantell SC, Cohen D, Model and experimental study of fiber motion in wet filament winding, Compos. Part A Appl. Sci. Manuf. 29(3) (1998) 251–263. 10.1016/S1359-835X(97)00091-2.

[101]. Cohen D, Mantell SC, Zhao L, The effect of fiber volume fraction on filament wound composite pressure vessel strength, Compos. B. Eng. 32(5) (2001) 413–429. 10.1016/S1359-8368(01)00009-9.

[102]. Zhao L, Mantell SC, Cohen D, McPeak R, Finite element modeling of the filament winding process, Compos. Struct. 52(3) (2001) 499–510. 10.1016/S0263-8223(01)00039-3.

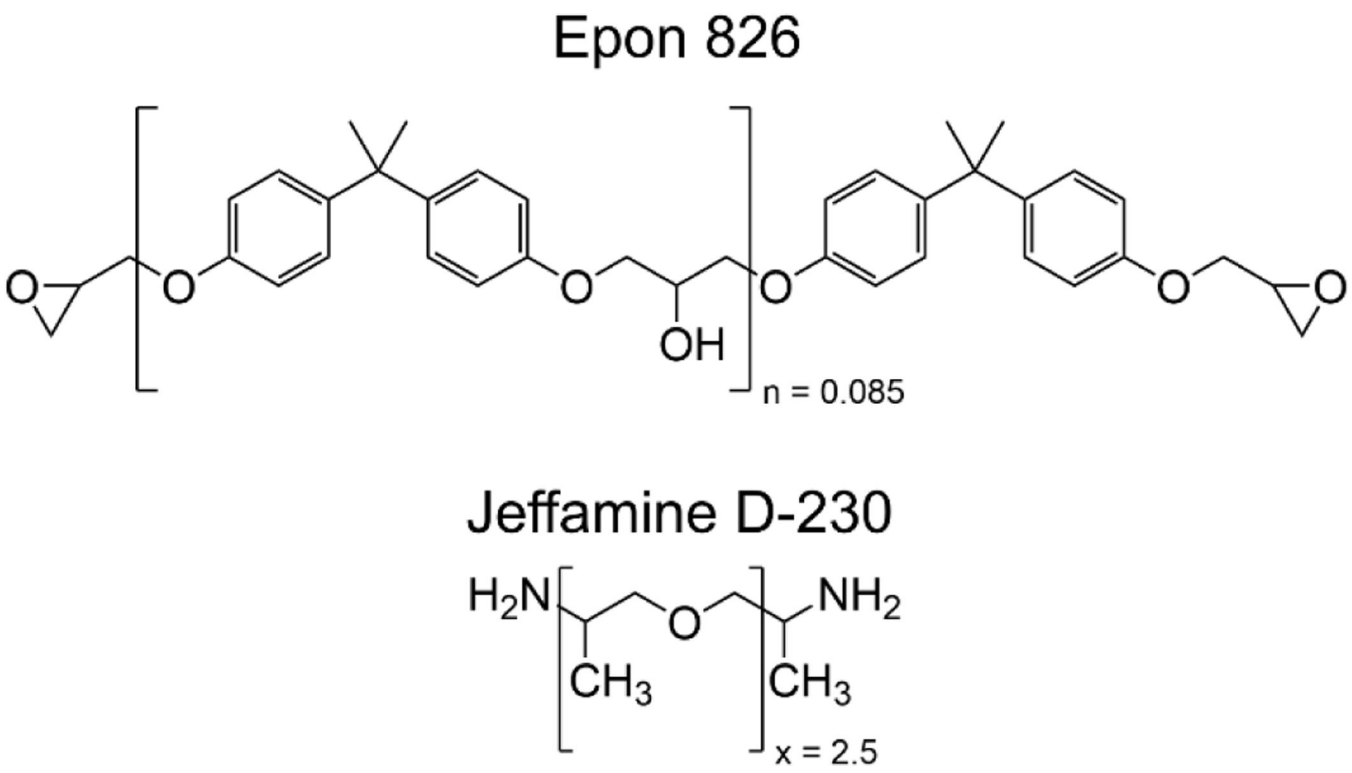

Figure 1:
Chemical structure of Epon 826 and Jeffamine D-230

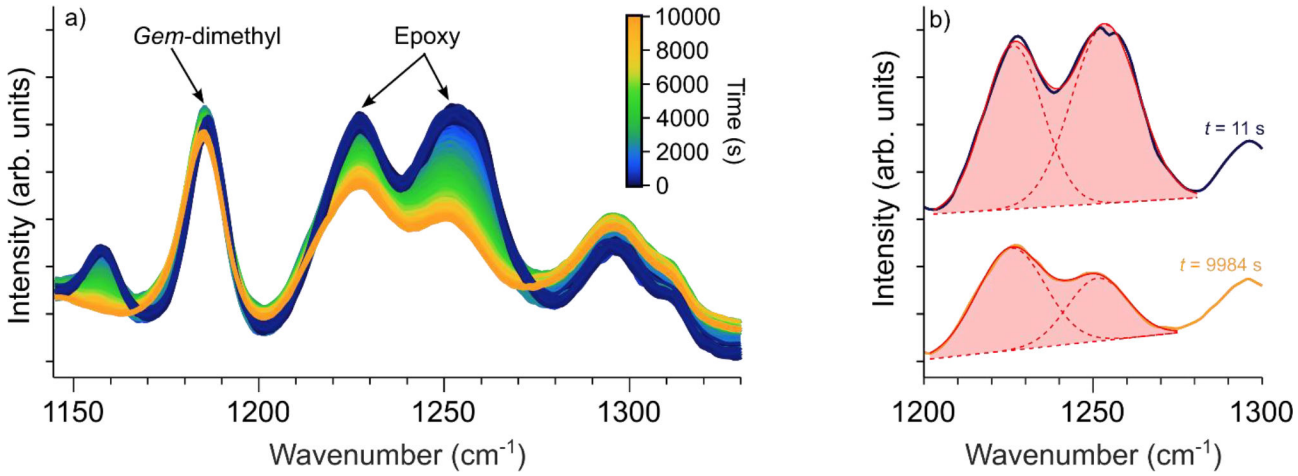

Figure 2:

Normalized Raman spectra of a neat resin curing at 70 °C. a) Spectra with labeled peaks of interest. b) Detail view of the selected epoxy responses between 1200 cm^{-1} and 1300 cm^{-1} with individual Gaussian fits and linear baseline (dotted lines), their sum (solid line), and the integrated intensity (shaded region). Curves have been vertically shifted to improve clarity.

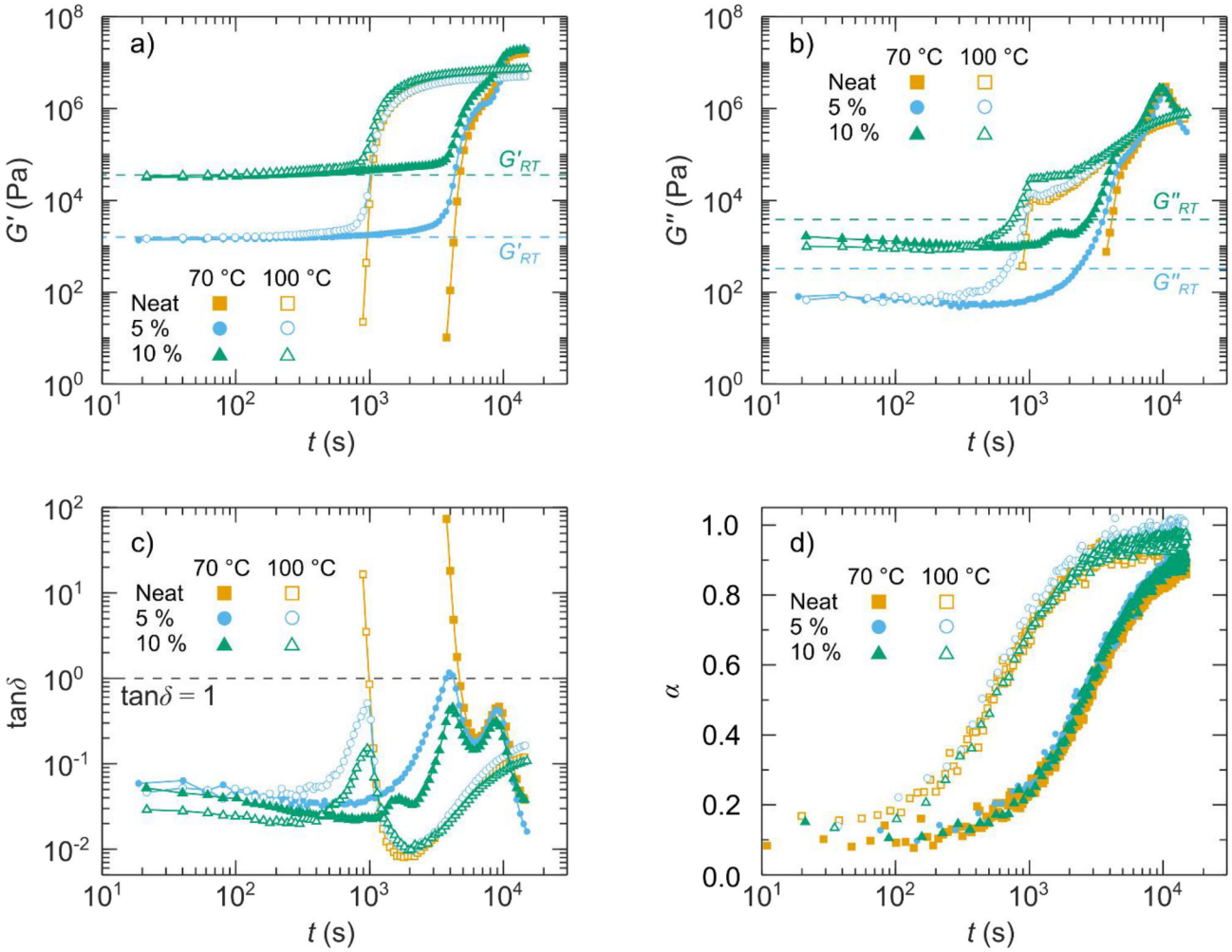

Figure 3:

Results of the SAOS experiments for each resin at each temperature. a) Storage modulus. b) Loss modulus. c) Loss tangent. (Duplicate experiments indicate the uncertainty in the SAOS measurements is less than 5 %. The uncertainty is insignificant on the logarithmic scale and is not shown to improve visibility of the data). d) Conversion (the maximum uncertainty in the conversion measurement was 0.0048 and is not shown to improve visibility). In a-c, the lines connect each datapoint taken, whereas the symbols represent the down-sampled data set to improve visibility of trends.

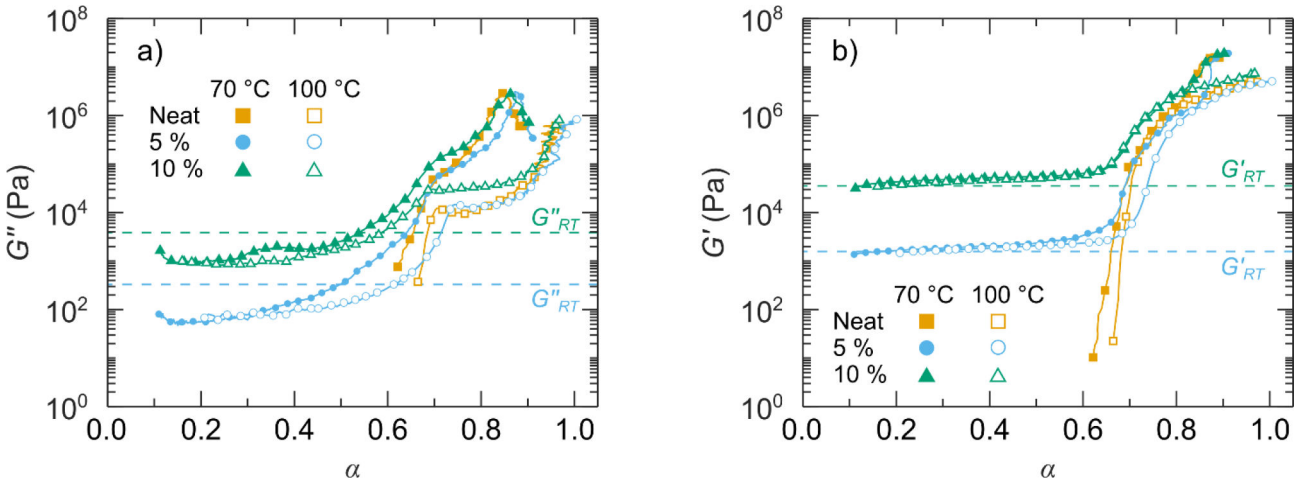

Figure 4:

Moduli as a function of conversion. a) Loss modulus. b) Storage modulus. The maximum uncertainty in the interpolated conversion measurement is 0.0036 and is not shown here to improve visibility.

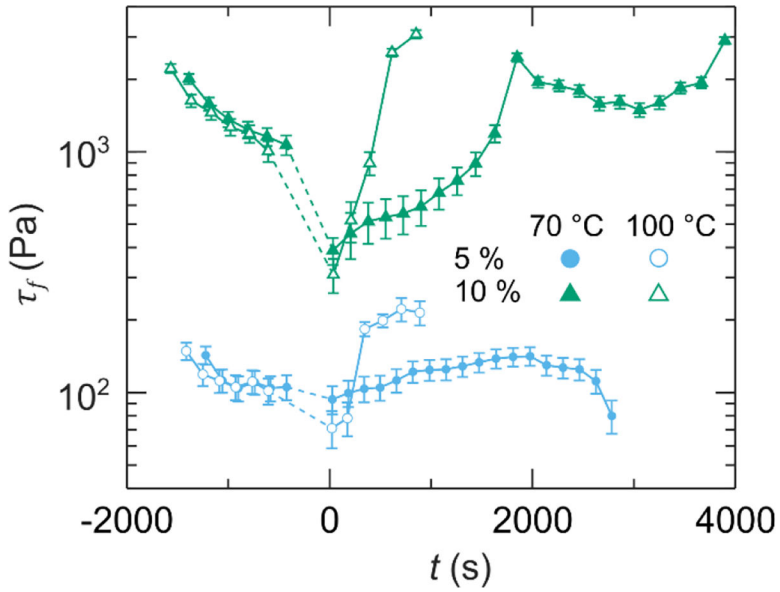

Figure 5:

Dynamic yield stress as a function of time. Negative time represents results before reaching the isothermal temperature. Dashed lines represent the ramp to the isothermal temperature. Positive time represents results after reaching the isothermal temperature. Error bars on the dynamic yield stress measurements represent the uncertainty which is defined as half of the difference between the experimentally applied stresses above and below the measured yield stress.

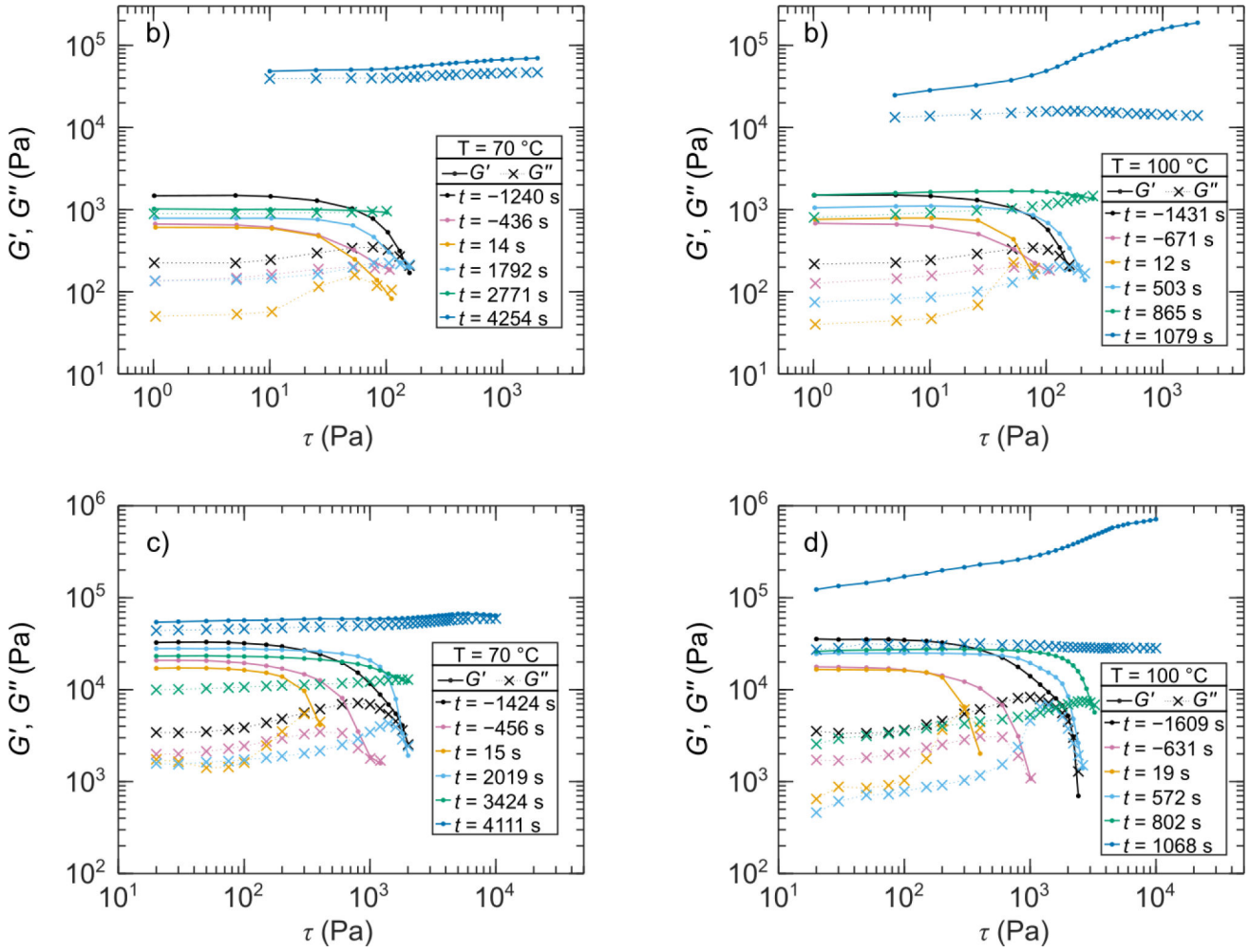

Figure 6:

Evolution of the stress amplitude sweeps at selected times. a) 5 % fumed silica resin cured at 70 °C. b) 5 % fumed silica resin cured at 100 °C. c) 10 % fumed silica resin cured at 70 °C. d) 10 % fumed silica resin cured at 100 °C. Note: "*t*" refers to the averaged time at which each sweep occurred. The sweeps labeled as negative time correspond to the first and final sweep at room temperature.

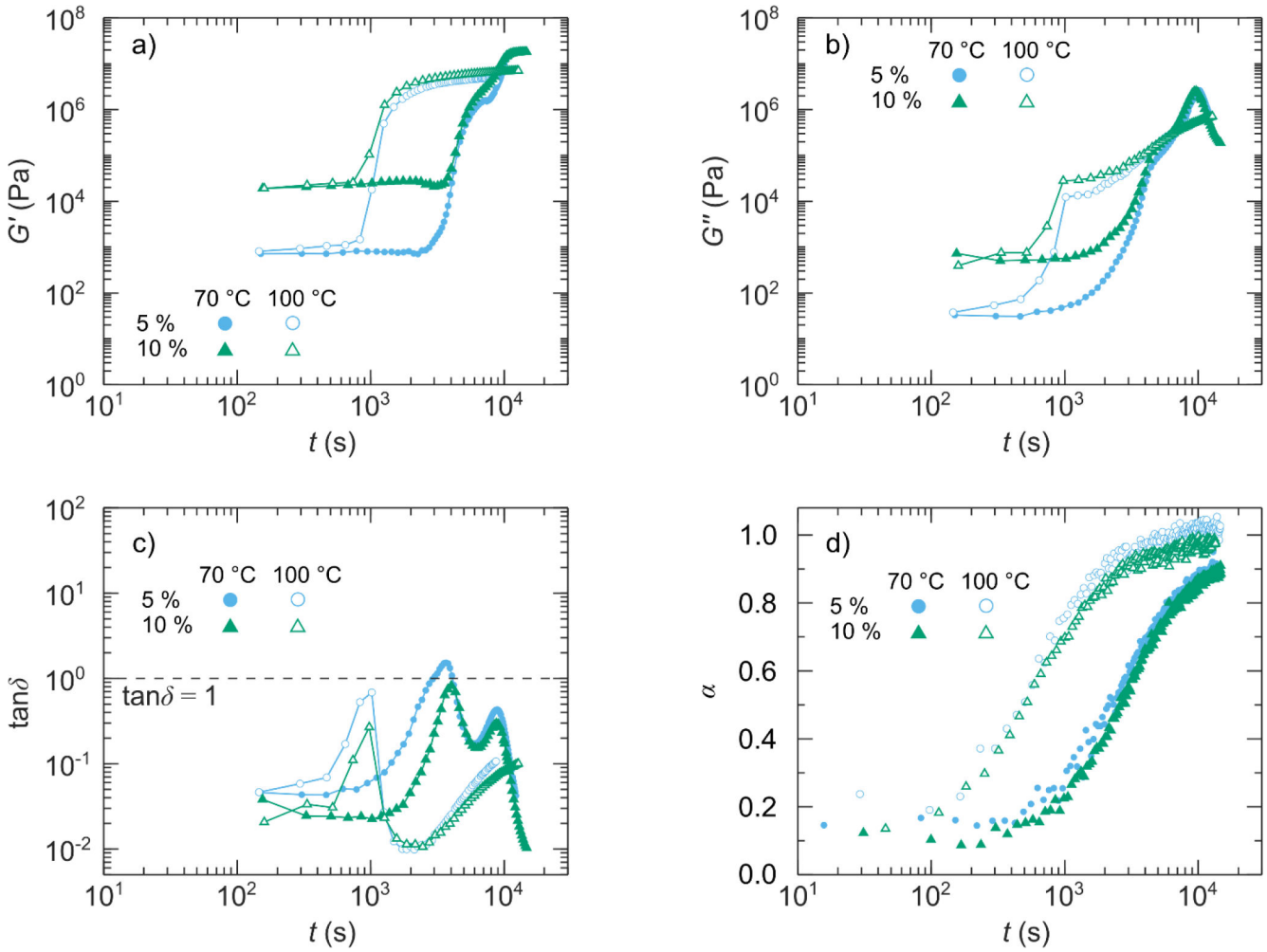

Figure 7:
SAOS results at the end of the recovery period during the stress sweep experiments. a) Storage modulus. b) Loss modulus. c) Loss tangent. d) Conversion.

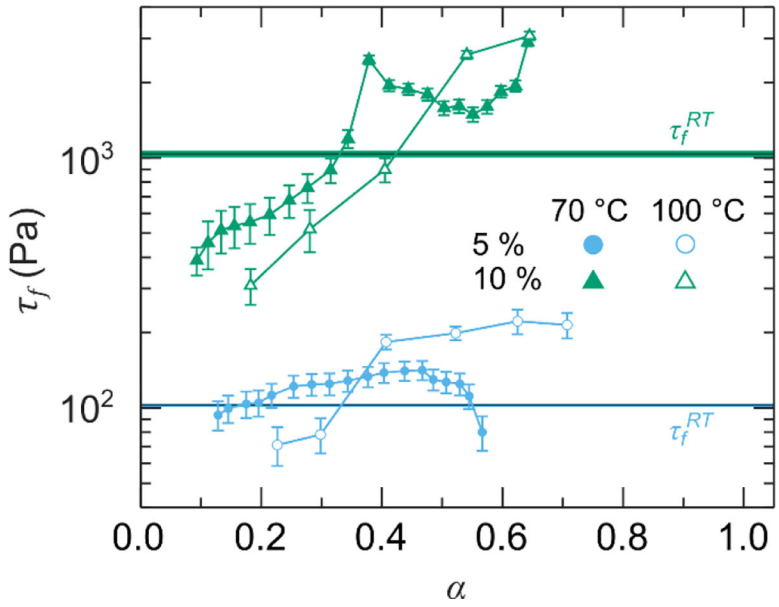

Figure 8:

Dynamic yield stress as a function of conversion. The maximum uncertainty in the interpolated conversion measurement is 0.0048 and is not shown here to improve visibility. The shaded region around τ_f^{RT} represents uncertainty.

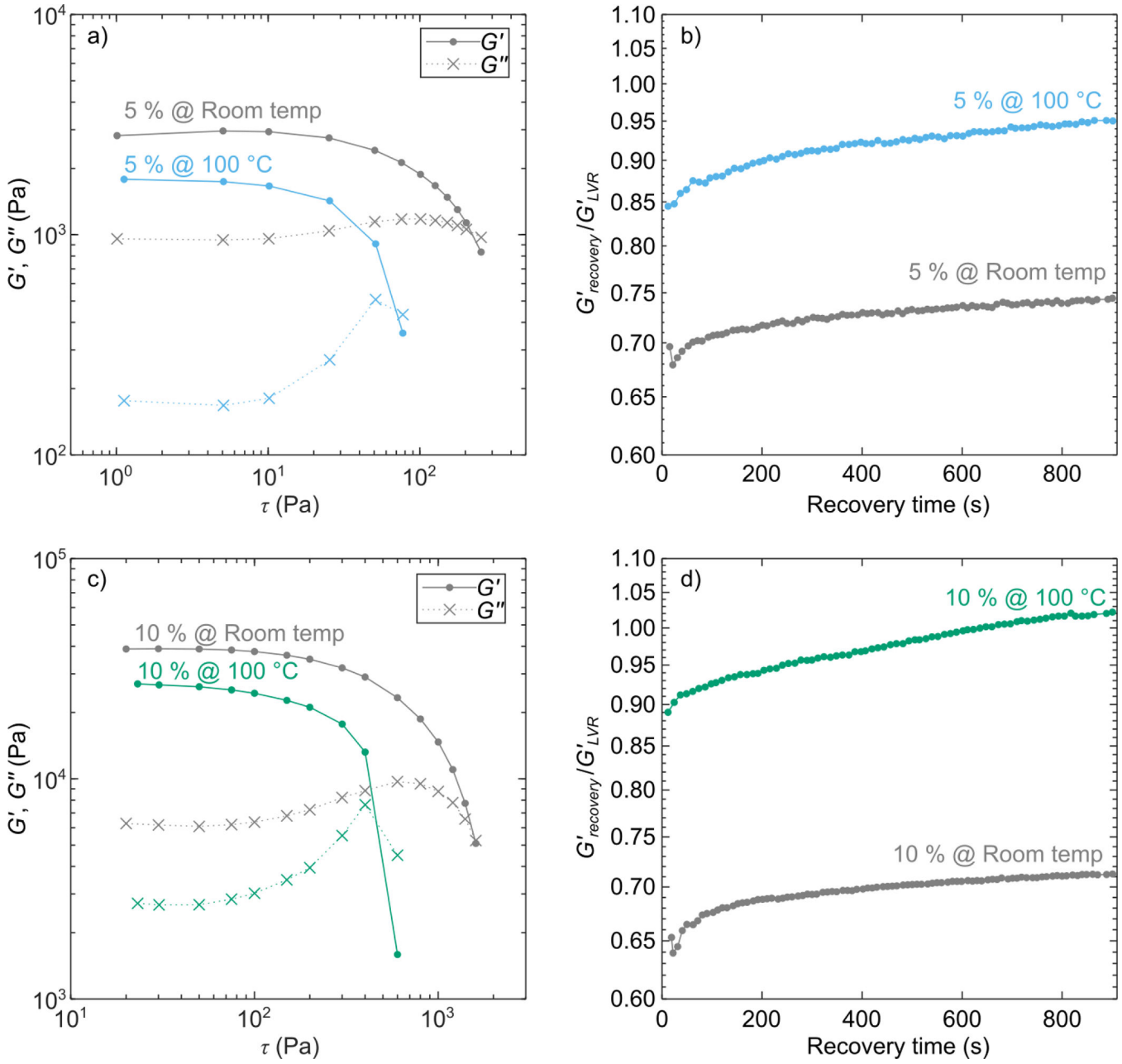

Figure 9:

Stress sweeps and subsequent normalized recovery on the filled resins without curing agent at room temperature and 100 °C. a) Stress sweeps of the resin with 5 % fumed silica. b) Recovery of the resin with 5 % fumed silica. c) Stress sweeps of the resin with 10 % fumed silica. d) Recovery of the resin with 10 % fumed silica.

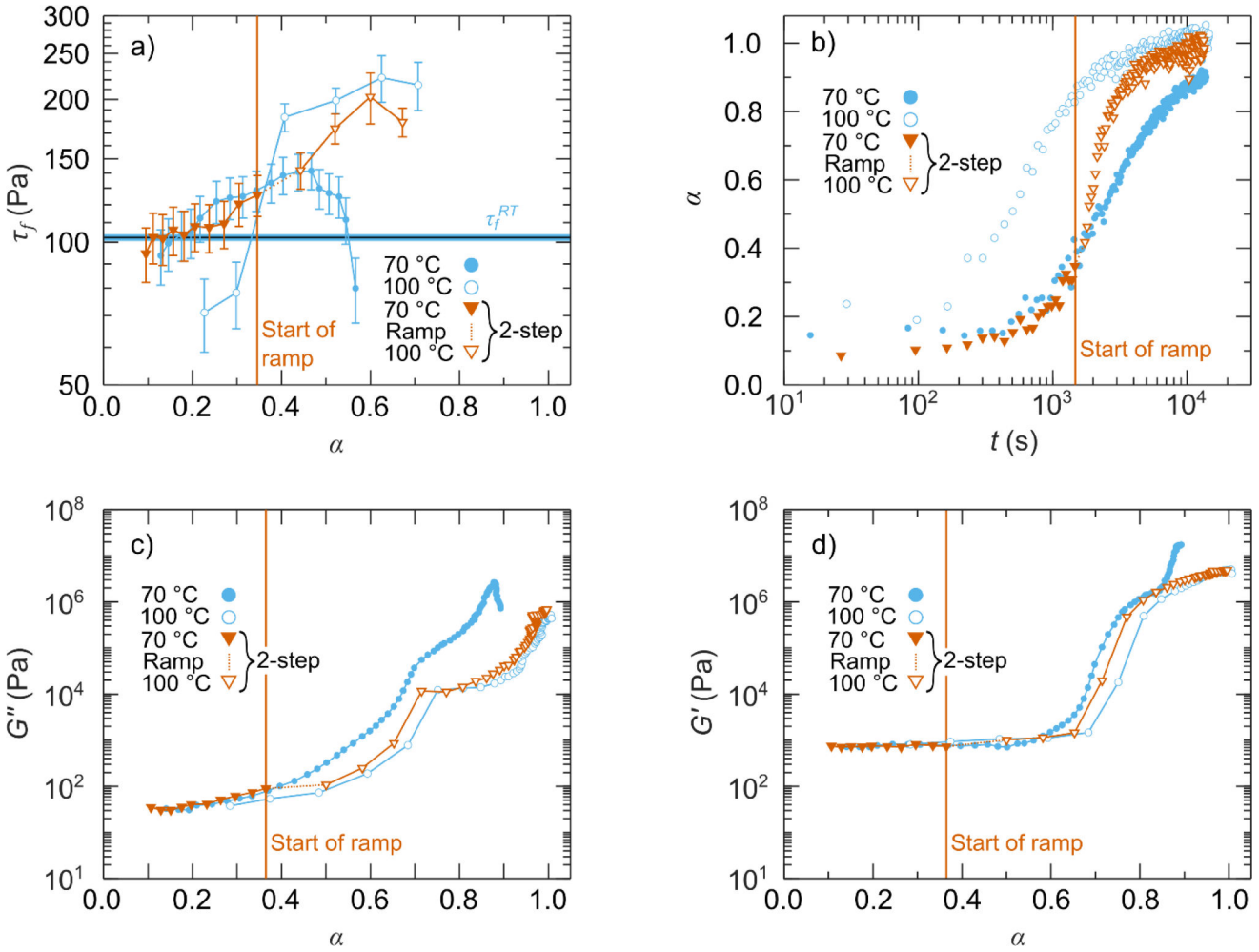

Figure 10:

Rheo-Raman results of the 5 % fumed silica resin cured using the two-step cure and under isothermal conditions (70 °C and 100 °C). a) Dynamic yield stress versus conversion (the maximum uncertainty in the interpolated conversion measurement is 0.0048 and is not shown here to improve visibility). b) Conversion versus time (the maximum uncertainty in the conversion measurement is 0.0059 and is not shown here to improve visibility). c) Loss modulus, as measured at the end of the recovery period, versus conversion (the maximum uncertainty in the conversion measurement is 0.0041 and is not shown here to improve visibility). d) Storage modulus, as measured at the end of the recovery period, versus conversion (the maximum uncertainty in the conversion measurement is 0.0041 and is not shown here to improve visibility).

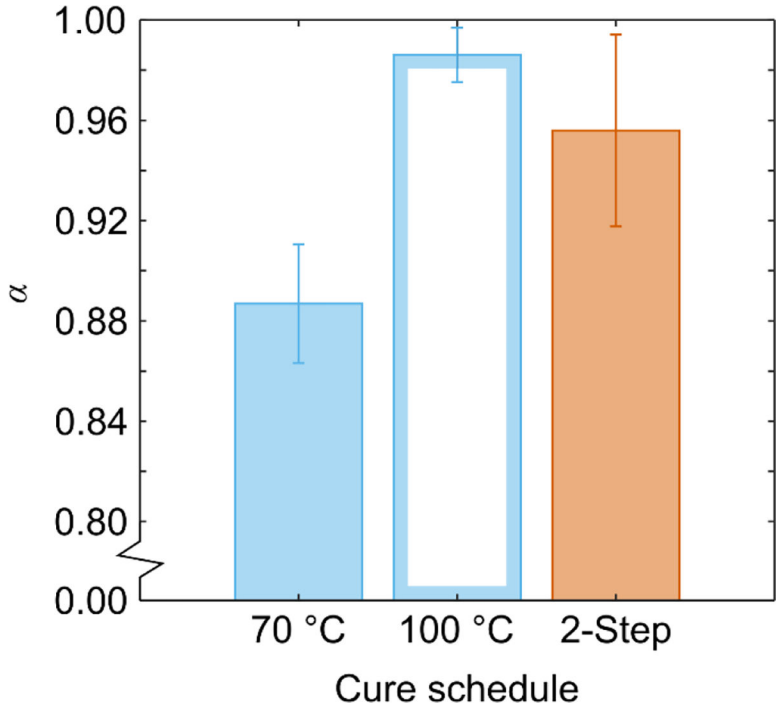

Figure 11:

Final conversion of samples cured in the oven. Error bars indicate the standard deviation based on two (for the 100 °C cure schedule) or three (for the 70 °C and 2-step schedules) samples.